



Article

Exploring the Effects of Synthetic and Postsynthetic Grinding on the Properties of the Spin Crossover Material $[\text{Fe}(\text{atrz})_3](\text{BF}_4)_2$ (atrz = 4-Amino-4*H*-1,2,4-Triazole)

Jed H. Askew ¹, David M. Pickup ¹, Gareth O. Lloyd ² , Alan V. Chadwick ¹ and Helena J. Shepherd ^{1,*} 

¹ School of Physical Sciences, University of Kent, Park Wood Rd, Canterbury CT2 7NH, UK; jha6@kent.ac.uk (J.H.A.); d.m.pickup@kent.ac.uk (D.M.P.); a.v.chadwick@kent.ac.uk (A.V.C.)

² School of Chemistry, Joseph Banks Laboratories, University of Lincoln, Lincoln LN6 7TS, UK; glloyd@lincoln.ac.uk

* Correspondence: h.j.shepherd@kent.ac.uk

Received: 19 August 2020; Accepted: 9 September 2020; Published: 15 September 2020



Abstract: The effects of mechanochemical synthesis and postsynthetic grinding on the spin crossover material $[\text{Fe}(\text{atrz})_3](\text{BF}_4)_2$ was examined in detail using a combination of X-ray diffraction, magnetometry, EXAFS and TEM. Mechanochemical synthesis yielded a different polymorph (β -phase) to the solution synthesised sample (α -phase), with a lower temperature spin crossover. Milling duration did not significantly affect this temperature but did result in the production of smaller nanoparticles with a narrower size distribution. It is also possible to convert from α - to the β -phase via postsynthetic grinding.

Keywords: spin crossover; mechanochemistry

1. Introduction

Spin crossover (SCO) is an area of significant research, primarily directed towards the development of switchable functional materials. SCO is characterised by the often reversible switching between high (HS) and low (LS) spin states as a result of changes in temperature, [1] pressure, [2] light irradiation [3] and both the introduction and removal of guest species [4]. Applications for SCO materials have been proposed in sensing, [5,6] display [7] and actuator technologies, [8,9] exploiting the spin-state induced changes in magnetic susceptibility, domain size, molecular structure and colour.

For optimum performance of molecular switches in many applications, molecular bistability (the ability to exist in two different states at the same temperature) is desirable. In SCO materials, these hysteretic effects can occur as a result of a high degree of cooperativity in the material whilst in the solid state [10]. A strongly cooperative system undergoes an abrupt transition and exhibits hysteresis on thermal cycling. Cooperativity is an inherent property of a system, and it depends on the strength of interactions between metal centres [11]. Therefore, isolated molecular systems connected by weak intermolecular bonding rarely exhibit cooperative spin transitions and bistability. However, multiple molecular systems which are designed to introduce strong intermolecular interactions have been reported, and in these systems, significant hysteresis has been observed [12,13]. In pursuit of increasingly cooperative SCO systems, coordination polymers have been suggested to possess great promise due to their extended connectivity through direct covalent bonding between active centres [14].

Previous studies into the modification of cooperativity in SCO systems have explored the effects of grinding various solution-synthesised SCO materials, which showed detrimental effects on the

properties, including an increase in residual HS state at low temperatures and a more gradual SCO. In some cases, an almost complete suppression of the SCO behaviour was identified [15,16]. However, in these reported examples, the samples were exposed to extremely harsh conditions, with prolonged milling in high energy planetary ball mills for several hours. The materials analysed were also molecular systems, which are inherently less cooperative and more susceptible to variations in crystallinity [16,17]. Recently, a significant change in SCO properties was reported as a result of postsynthetic grinding, attributed to a 'mechanochemical recrystallization' process [18].

One of the most widely researched family of SCO materials is that based on the 4-R-1,2,4-triazole (R-trz) ligands, with the general formula $[\text{Fe}(\text{R-trz})_3]\text{A}_x \cdot n\text{H}_2\text{O}$ (R = H, NH_2 , alkyl, other functional groups and A = anion). This family is of interest in part due to SCO dependence on both R-group and anions; with significant variation (160–385 K) in the transition temperatures reported. The materials often show high cooperativity and frequently undergo high temperature transitions [19]. Additionally, the ease of processing as nanoparticles and retention of SCO in small particles makes the family an interesting candidate for many potential applications. This family forms 1-D chains of Fe^{2+} centres triply bridged by triazole ligands, thus defining an extended coordination network. This results in many members of the family displaying abrupt SCO transitions and wide hysteresis [20,21]. The family is known to be highly sensitive to the presence of solvents, with often has dramatic effects on SCO properties [22]. However, standard synthetic approaches require the use of aqueous and/or methanolic solution reaction conditions.

Several studies of $[\text{Fe}(\text{atrz})_3](\text{BF}_4)_2$, where atrz = 4-amino-4H-1,2,4-triazole have been reported to date, and literature available on solution-synthesised samples, present a complex situation, with multiple reported SCO temperature ranges identified [19,23–25] and significant potential for solvent effects [26]. The previously reported literature values for the SCO temperature of $[\text{Fe}(\text{atrz})_3](\text{BF}_4)_2$ were first described by Kahn [23], then confirmed by both Roubeau [19] and Grosjean, [27] with $T_{1/2}\uparrow = 260$ K and $T_{1/2}\downarrow = 250$ K. A second phase of $[\text{Fe}(\text{atrz})_3](\text{BF}_4)_2$ with $T_{1/2}\uparrow = 245$ K and $T_{1/2}\downarrow = 239$ K was also identified by Grosjean [27]. However, in their study, they were only able to observe a polycrystalline mixture of phases and were unable to isolate either as a pure phase. The phase with a higher transition temperature, hereby denoted the ' α -phase', was significantly more crystalline and allowed for structural analysis. By contrast, the form with a lower transition temperature, hereby denoted the ' β -phase', was weakly crystalline. It is worth noting the possibility of a third SCO transition temperature, which has been previously reported in the literature with $T_{1/2}\uparrow = 312$ K and $T_{1/2}\downarrow = 302$ K [24]. However, in that report, the difference in transition temperature was noted, but no explanation for the difference was suggested. No subsequent literature on this complex has shown a transition with these higher transition temperatures.

Recently, we reported the mechanochemical synthesis of a variety of SCO materials, yielding products that maintained cooperativity and crystallinity [28] and the postsynthetic modification of SCO materials using mechanochemical solid state metathesis [29]. Maintaining cooperativity and crystallinity was attributed to shorter reaction times, carried out by lower energy manual grinding. A recent report on the effect of postsynthetic grinding on the chemically similar material, $[\text{Fe}(\text{trz})(\text{Htrz})_2](\text{BF}_4)$ (where trz = 1,2,4-triazolato and Htrz = 1,2,4-4H-triazole), showed that increased duration of grinding caused changes in the SCO temperature, which was attributed to a 'mechanochemical recrystallisation' process [18].

Herein, we explore the effects of synthetic and postsynthetic grinding on $[\text{Fe}(\text{atrz})_3](\text{BF}_4)_2$. By direct comparison with solution synthesised samples, we explored the reported factors which can affect SCO properties, including solvent effects, amorphisation, particle size and morphology using a variety of techniques including SQUID magnetometry, PXRD, TGA, Fe-edge EXAFS and TEM. We also addressed the potential for polymorph discovery inaccessible via solution-state synthetic approaches.

2. Experimental

All reagents were purchased from Fisher Scientific and were used as received without additional purification. All mechanochemical experiments were conducted in air under ambient conditions using a glass pestle and mortar.

Compounds synthesised by mechanochemistry were prepared using Iron(II) tetrafluoroborate (1 eqv) and 4-amino-4H-1,2,4-triazole (atrz, 3 eqv). Grinding in a pestle and mortar for 10 min under ambient conditions yielded **1-Mech**. Ball milled samples were prepared in a Retsch MM400 mill using Teflon cups and two 7 mm Teflon balls (≈ 0.21 g each) operating at a frequency of 25 Hz for either 10 min (yielding compound **1-BM10**) or 90 min (yielding **1-BM90**). No washing was carried out on mechanically prepared samples.

$[\text{Fe}(\text{atrz})_3](\text{BF}_4)_2$ (**1-Sol**) was prepared by dropwise addition of Iron(II) tetrafluoroborate hexahydrate (0.94 g, 2.8 mM) and L-ascorbic acid (0.05 g) in methanol (100 mL) to 4-amino-4H-1,2,4-triazole (0.7 g, 8.3 mM) in methanol (100 mL). The mixture was stirred under ambient conditions overnight. The white precipitate was collected by filtration and washed with water and methanol then dried overnight under vacuum yielding a fine white powder (0.88 g, 64%). Postsynthetic grinding of **1-Sol** was undertaken in a pestle and mortar and manually ground for 10 min (yielding **1-Sol-10**) and 30 min (yielding **1-Sol-30**). Between measurements, samples were stored in sealed sample vials.

CAUTION: Do not use mechanochemical techniques for the preparation of potentially explosive materials. Perchlorate salts and tetrazole ligands are sometimes used in SCO research. Both of these have the potential to explode when handled dry, particularly on contact or grinding, and thus should not be used in routine mechanochemical experiments.

3. Instrumentation

Magnetic susceptibility measurements were carried out using a Quantum Design MPMS SQUID magnetometer. Temperature dependent measurements were made using a 1000 Oe magnetic field across the stated temperature ranges, while ramping the temperature at a rate of 2 K min^{-1} .

Powder X-ray diffraction (PXRD) data were collected using a Panalytical X'Pert3 using Cu K α radiation, $\lambda = 1.54051$, with a power rating 40 kV and 20 mA. The 2θ range $5\text{--}40^\circ$ was recorded with continuous scanning using a step size 0.0041778° with 400 s exposure per step. Samples were mounted on a silicon crystal sample holder.

Thermogravimetric Analysis (TGA) was carried out using a Netzsch Luxx STA 409 PC, scanning the range $25 \rightarrow 500^\circ \text{C}$ with a heating rate of 5 K/min . Differential scanning calorimetry (DSC) was performed using a Netzsch Phox DSC 200 PC scanning between the stated temperature ranges with a heating rate of 10 K/min ; a minimum of 3 cycles were performed with transition temperatures determined using the second cycles.

XAFS data were collected for Fe K-edge at room temperature on beam line B18 at the Diamond Light Source. Data collection used transmission mode with ion chamber detectors. Continuous scanning (QEXAFS) was employed; an individual scan required 180 s, and several scans were performed to improve the signal-to-noise ratio. The synchrotron energy and current were 3 GeV and 300 mA, respectively. The beam size at the sample was 700×700 microns. Powdered samples were mixed with polyvinylpyrrolidone (PVP) as a diluent and pressed into 13 mm diameter pellets. The spectra were normalised in Athena and fitted to scattering models in R-space produced by FEFF in Artemis.

Transmission Electron Microscopy (TEM) was performed using a Jeol 1,230,120 kV Transmission Electron Microscope equipped with a Gatan One View 16 mp camera with automatic drift correction. Samples were prepared by adapting the method described by Petri-Fink et al. [30]. An amount of 10 mg was added to MilliQ water (10 mL) and sonicated for 30 min. Bovine Serum Albumin (BSA) (15 mg) was dissolved in MilliQ water (10 mL) and sonicated for 15 min. An aliquot of the BSA solution (100 μL) was added to an aliquot of the compound solution (100 μL) and sonicated for an additional 15 min. A total of 600 mesh copper grids purchased from Agar Scientific were coated in ~ 70 nm of formvar and ~ 5 nm of

evaporated carbon using a QuorumQ150T ES Evaporative coater. Aliquots of 2 μL of the sample/BSA solution were deposited on the copper grids and vacuum dried at 30 $^{\circ}\text{C}$ for 30 min.

4. Results and Discussion

4.1. Synthetic Grinding

$[\text{Fe}(\text{atrz})_3](\text{BF}_4)_2$ (compound **1**) was synthesised using four different synthetic routes. **1-Sol** was prepared by a solution-based method. **1-Mech** was prepared by manual grinding of the reagents in a pestle and mortar. **1-BM10** and **1-BM90** were synthesised using a ball mill for 10 and 90 min, respectively; a full description of the procedures is presented in experimental data. All four synthetic routes yielded a white powder which underwent a HS to LS transition on cooling. The variable temperature magnetic properties for each product were recorded using SQUID magnetometry, as shown in Figure 1a. Only one heating cycle is shown for clarity, full plots are available in the Supplementary Materials, and characteristic properties are shown in Table 1. **1-Sol** exhibited a relatively gradual transition with a ‘smoothness’ of 39 K, $T_{1/2}\uparrow = 251$ K and $T_{1/2}\downarrow = 250$ K, consistent with previously reported literature values [19,23,27] which exhibited SCO with $T_{1/2}\uparrow = 260$ K and $T_{1/2}\downarrow = 250$ K. Smoothness is defined as the difference in the temperatures for which 80% and 20% of the complexes are in the HS state [28]. The absence of significant hysteresis in **1-Sol** is discussed in more detail below.

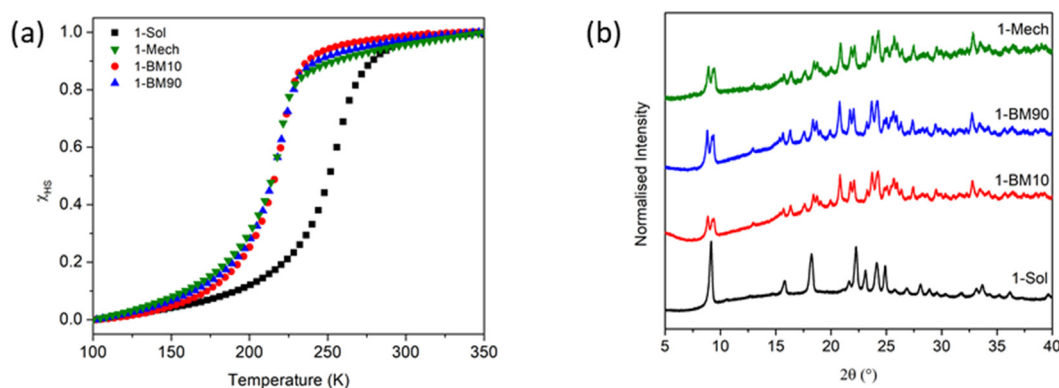


Figure 1. (a) Normalised $\chi_M T$ vs. temperature plots, second heating cycles, for **1-Sol** (■), **1-Mech** (▼), **1-BM10** (●) and **1-BM90** (▲). (b) Normalised PXRD for **1-Sol**, **1-Mech**, **1-BM10** and **1-BM90**.

Table 1. Spin crossover (SCO) properties determined by SQUID magnetometry for **1-Sol**, **1-Mech**, **1-BM10** and **1-BM90**.

Sample	$T_{1/2}\uparrow$ (K)	$T_{1/2}\downarrow$ (K)	ΔT (K)	‘Smoothness’
1-Sol	251	250	1	39
1-Mech	215	212	3	31
1-BM10	216	212	4	30
1-BM90	215	211	4	30

All three mechanically synthesised samples underwent SCO at a significantly lower temperature (>30 K) than **1-Sol**. **1-Mech** underwent a more abrupt transition than **1-Sol** (‘Smoothness’ = 31 K) with $T_{1/2}\uparrow = 215$ K and $T_{1/2}\downarrow = 212$ K, consistent with the values previously reported for the β -phase [27]. **1-BM10** also showed a more abrupt transition than **1-Sol** (‘Smoothness’ = 30 K) with transition temperatures comparable to **1-Mech** ($T_{1/2}\uparrow = 216$ K and $T_{1/2}\downarrow = 212$ K). Finally, **1-BM90** exhibited similar transition properties to other mechanically synthesised samples (‘Smoothness’ = 30 K) centred on $T_{1/2}\uparrow = 215$ K and $T_{1/2}\downarrow = 211$ K. In all four of the samples reported here, only a single SCO event was apparent in the magnetic data, strongly indicating the presence of only a single SCO-active phase in each case.

Powder diffraction patterns of each sample are shown in Figure 1b. The pattern for **1-Sol** closely resembles that described by Grosjean, [27] thus confirming the solution-state formation of the α -phase. However, the patterns for all three mechanically synthesised samples are virtually identical to each other but significantly different to the solution synthesised sample. In the study by Grosjean, a number of peaks present in the pattern of the mixed phase material are outside of the proposed fit of the α -phase. These additional peaks correlate well with the patterns collected for **1-Mech**, **1-BM10** and **1-BM90**, therefore, suggesting that the β -phase alone is produced by mechanochemical synthesis.

The Fourier transform of Fe-edge EXAFS data are shown in Figure 2. The data were collected at room temperature, where the complex is in the HS state, in both α and β phases. Data show that all of the samples have the same short-range order. The peak at 2.20(1) Å corresponds to the Fe-N distance, consistent with a Fe^{2+} HS species [31]. The following peaks represent the Fe-C (3.17(1) Å), Fe-C (3.18(1) Å) and Fe-Fe (3.90(5) Å) shells. It is not possible to observe Fe-Fe-Fe multiple scattering in any of the samples of compound 1; the absence of such a peak in the HS state is expected and has been discussed extensively in literature, owing to a greater Fe-N bond length distribution as a result of the degenerate $^5\text{T}_{1g}$ state [31,32]. The Debye–Waller factors ($2\sigma^2$), which are the measure of the thermal and static disorder within a shell, show no significant variation between samples. This suggests that mechanical synthesis or BM do not introduce significant disorder into the structure compared to solution synthesis. In all four cases, the amount of amorphisation is comparable; differences between the values are within the error of the measurement. Therefore, synthesis via mechanochemistry does not introduce amorphisation into this system—even after prolonged grinding in a ball mill as seen in **1-BM90**. Full fitting data are available in the Supplementary Materials.

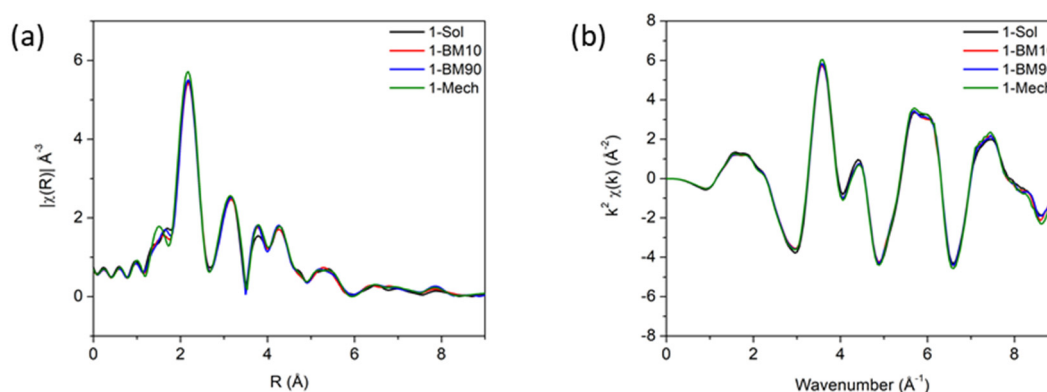


Figure 2. (a) k^3 weighted pseudo-radial distribution function of Fe K-edge spectra for **1-Sol**, **1-BM10**, **1-BM90** and **1-Mech**. (b) Combined Fe-Edge K Space EXAFS spectrum (k^3 weighted) for **1-Sol**, **1-BM10**, **1-BM90** and **1-Mech**. The difference at 3.8 Å is attributed to a fitting artefact and discussed further in the Supplementary Materials.

Solvent effects on SCO properties were explored by TGA. The mechanically synthesised samples showed a slight variation in mass loss with **1-Mech** losing 2.3% (0.6 eqv. H_2O), **1-BM90** losing 2.6% (0.7 eqv. H_2O) and **1-BM10** losing the least at 0.9% (0.2 eqv. H_2O). The difference in water content for mechanically synthesised samples has proved insignificant with regard to their SCO properties. The water content for **1-Sol** was slightly greater than **1-BM10** at 1.5% (0.4 eqv. H_2O), but still remained lower than both **1-Mech** and **1-BM90**; all calculated mass loss remained within the potential error of the calculation. As such, the differences in magnetic properties are not attributed to differences in hydration, and previously reported effects of hydration are not observed in these samples. The amount of water varied between samples without affecting the properties, and as such, this water was likely adsorbed onto the surface of the material rather than a stoichiometric component of the complex. Full plots are shown in the Supplementary Materials.

Particle size and morphology were determined by TEM, as shown in Figures 3 and 4. In all four samples, the particles had a spherical morphology. Particles of **1-Sol** were determined to be 48 ± 22 nm

in diameter, and **1-Mech** particles were measured at 53 ± 20 nm. Both **1-Sol** and **1-Mech** showed large particle size distribution with similar particle sizes, strongly indicating that the differences in magnetic properties are not due to size effects. Both **1-BM10** and **1-BM90** showed smaller particle sizes than **1-Sol**, with **1-BM10** = 27 ± 11 nm and **1-BM90** = 22 ± 7 nm. The variation in particle size observed in the mechanically synthesised samples is not accompanied by differences in magnetic properties, aside from the irreversible first cycle observed for **1-BM10** which is attributed to the often observed ‘run-in’ effect in these systems [33]. However, longer grinding of the samples led to a slight decrease in both particle size and particle size distribution which remained within the potential error, whilst maintaining magnetic properties.

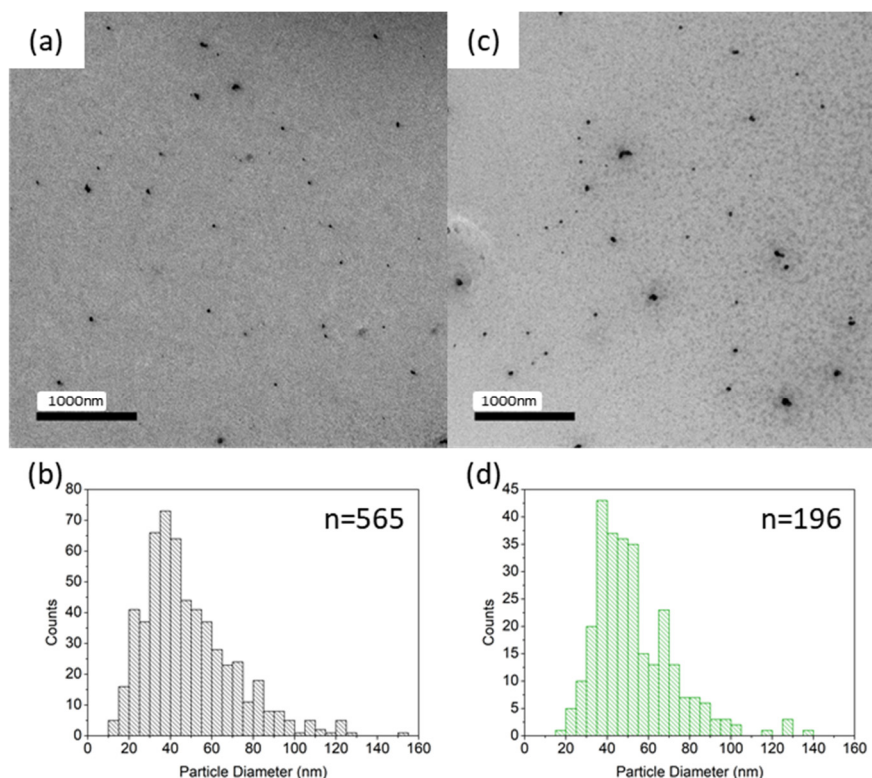


Figure 3. (a) Representative TEM image for compound **1-Sol**: additional images available in the Supplementary Materials. (b) Particle length distribution for compound **1-Sol**, where $n = 565$. (c) Representative TEM image for compound **1-Mech**: additional images available in the Supplementary Materials. (d) Particle length distribution for compound **1-Mech**, where $n = 196$.

4.2. PostSynthetic Grinding

Conversion between the two phases of $[\text{Fe}(\text{atrz})_3](\text{BF}_4)_2$ was attempted by postsynthetic grinding of a sample of **1-Sol** for 10 min, in an attempt to replicate the conditions of the synthetic grinding process of **1-Mech** (yielding **1-Sol-10**). The magnetic properties of **1-Sol-10** were investigated as shown in Figure 5a. After grinding, **1-Sol-10** displayed a two-step transition, as indicated by the first derivative (Figure 5c) with the first-step $T_{1/2\uparrow} = T_{1/2\downarrow} = 212$ K representing $\approx 60\%$ of the total transition, and the second-step $T_{1/2\uparrow} = T_{1/2\downarrow} = 252$ K representing the remaining $\approx 40\%$. The former is consistent with the transition temperature measured for the β -phase in the mechanochemically synthesised samples (**1-Mech**, **1-BM10** and **1-BM90**), and the latter is similar in temperature to **1-Sol** prior to grinding; the α -phase. **1-Sol-10** was ground for an additional 20 min, yielding **1-Sol-30**. **1-Sol-30** displayed two-step SCO with the first-step consistent with **1-Sol-10**, $T_{1/2\uparrow} = T_{1/2\downarrow} = 212$ K representing an increased proportion of the transition (75%) and the second-step $T_{1/2\uparrow} = T_{1/2\downarrow} = 252$ K representing the remaining 25%, as shown in Figure 5b, with first the derivative included in Figure 5d to emphasise two-step transition. Thus, as grinding time increases, the conversion of the α -phase into the β -phase

increases. While it may be possible to achieve a complete conversion of the α -phase into the β -phase, it would require a longer grinding duration than employed here.

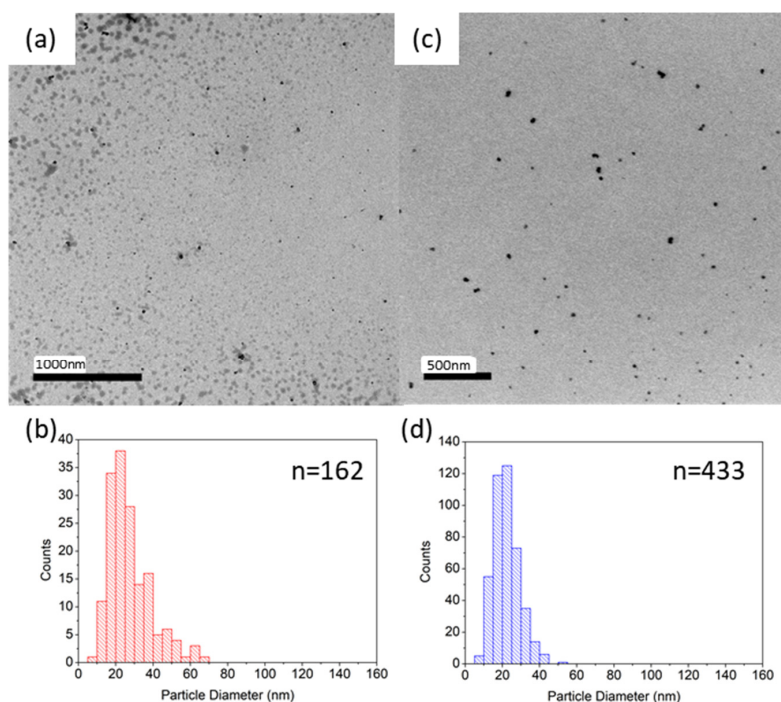


Figure 4. (a) Representative TEM image for compound **1-BM10**: additional images available in Supplementary Materials. (b) Particle length distribution for compound **1-BM10**, where $n = 162$. (c) Representative TEM image for compound **1-BM90**: additional images available in the Supplementary Materials. (d) Particle length distribution for compound **1-BM90**, where $n = 433$.

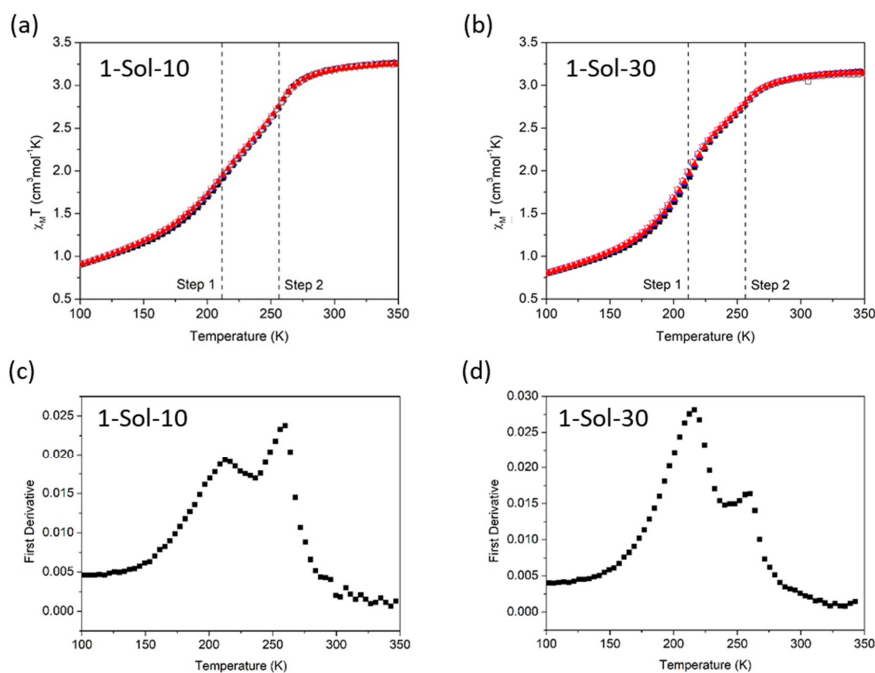


Figure 5. Plots of $\chi_M T$ vs. T for compound three cycles, with the stepped transitions indicated by dashed lines. First cycle: heating \blacksquare , cooling \square ; second cycle: heating \blacktriangle , cooling \triangle ; third cycle: heating \blacktriangledown and cooling \triangledown (a) **1-Sol-10** (b) **1-Sol-30**. First derivative of 2nd heating cycle. (c) **1-Sol-10** and (d) **1-Sol-30**.

Due to the solution-state synthesis of **1-Sol** including a washing step to remove impurities and both **1-Sol-10** and **1-Sol-30** originating from the same sample, the absolute X_{MT} values and their relative changes can be used to investigate the change in residual HS fraction induced by postsynthetic grinding. The residual HS fraction remaining at 100 K for **1-Sol** was a value of $0.6 \text{ cm}^3 \text{ mol}^{-1} \text{ K}$ which slightly increased in **1-Sol-10** with a $0.9 \text{ cm}^3 \text{ mol}^{-1} \text{ K}$ and a similar value in **1-Sol-30** ($0.8 \text{ cm}^3 \text{ mol}^{-1} \text{ K}$). It is worth noting that the residual HS fractions for **1-Mech** ($0.4 \text{ cm}^3 \text{ mol}^{-1} \text{ K}$), **1-BM10** ($0.2 \text{ cm}^3 \text{ mol}^{-1} \text{ K}$) and **1-BM90** ($0.3 \text{ cm}^3 \text{ mol}^{-1} \text{ K}$) do not indicate that the β -phase inherently contains a higher residual HS fraction. Therefore, this increase in residual HS fraction is likely attributed to a decrease in particle size caused by the grinding process and not an inherent property of the β -phase. Further investigation into the effects of changing grinding conditions is ongoing.

The effect of postsynthetic grinding was monitored using powder diffraction, as shown in Figure 6, which showed the structure remained mostly unchanged after grinding for 10 min (**1-Sol-10**). The majority of the peaks remained consistent with the exception of the presence of a shoulder on the peak at 8° and the appearance of two peaks at 13° and 21° . Continued grinding for a total of 30 min increased the size of the shoulder at 8° and the peaks at 13° and 21° . The peaks and peak splitting present after 30 min of grinding are consistent with the pattern collected for the β -phase. Grinding **1-Sol** also decreased the signal-noise ratio, which is attributed to a lower crystallinity for the β -phase, as previously discussed by Grosjean [27]. The pattern for **1-Sol-30** appeared to be a mixture of the patterns for **1-Sol** and **1-Mech**.

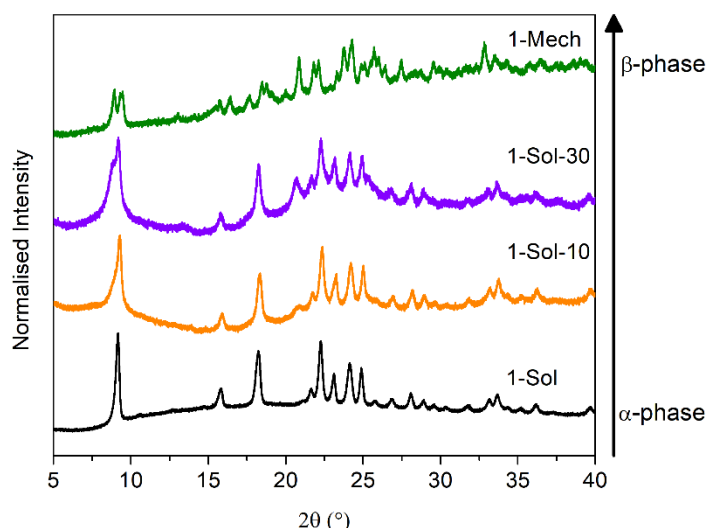


Figure 6. Normalised PXRD for **1-Mech**, **1-Sol-30**, **1-Sol-10** and **1-Sol**.

The degree of hydration was investigated by TGA analysis. At 150°C , **1-Sol-10** lost 3.5% (0.9 eqv. H_2O) and **1-Sol-30** lost 4.2% (1.0 eqv. H_2O). Both **1-Sol-10** and **1-Sol-30** showed a mass loss greater than **1-Sol** indicating the moisture content increased during the grinding process. This may indicate a link between moisture content and the polymorph identified. However, initial comparisons between **1-Sol** and the three mechanically prepared samples indicated that water content was not a significant factor affecting the form observed, as shown in Table 2. Therefore, the increased water content observed for **1-Sol-10** and **1-Sol-30** is tentatively attributed to external factors, such as variation in environmental humidity. Full TGA plots are presented in the Supplementary Materials.

Table 2. Mass loss at 150 °C determined by TGA with corresponding equivalence of H₂O per complex, for 1-Mech, 1-BM10, 1-BM90, 1-Sol, 1-Sol-10 and 1-Sol-30.

Sample	Mass Loss (%)	Stoichiometric Ratio of Water
1-Mech	2.3	0.6
1-BM10	0.9	0.2
1-BM90	2.6	0.7
1-Sol	1.5	0.4
1-Sol-10	3.5	0.9
1-Sol-30	4.2	1.0

5. Conclusions

Compound 1 was synthesised by four methods: a standard solution-state approach (**1-Sol**), manual grinding in a pestle and mortar (**1-Mech**) and by ball-mill for two different durations (**1-BM10** and **1-BM90**). In previous literature, only one form of [Fe(atrz)₃](BF₄)₂ has been fully characterised, hereby named the α -phase, although the possibility of a second phase (β) had been previously identified [23,27]. **1-Sol** exhibited magnetic properties consistent with previously reported literature for the α -phase ($T_{1/2}\uparrow = 251$ K, $T_{1/2}\downarrow = 250$ K). Mechanochemical synthesis yielded a significantly different product to the solution-synthesised sample. The product yielded by all three mechanical approaches displayed similar magnetic properties (based around $T_{1/2}\uparrow = 215$ K, $T_{1/2}\downarrow = 212$ K). Unlike previous literature reports on a chemically similar material, [Fe(trz)(Htrz)₂](BF₄) (where trz = 1,2,4-triazolato and Htrz = 1,2,4-4H-triazole), the increased milling duration in **1-BM90**, compared to **1-Mech** and **1-BM10**, did not significantly alter the transition temperature [18]. Despite [Fe(trz)(Htrz)₂](BF₄) and [Fe(atrz)₃](BF₄)₂ showing very similar chemical structures, the effect of mechanochemistry on each system was significantly different, emphasising that there is still great potential for the technique in tuning the properties of SCO materials.

PXRD confirmed the same structure for all mechanical products but a different structure to the solution sample. However, EXAFS analysis indicated the same short-range one-dimensional chain structure for both sets of samples with similar degrees of amorphisation. Water content was analysed by TGA, providing no evidence that moisture content affected the phase synthesised nor the SCO properties of that phase. The potential for size effects was explored by TEM: **1-Sol** and **1-Mech** were shown to have particles of similar size (**1-Sol** = 48 ± 22 nm and **1-Mech** = 53 ± 20 nm), proving that the differences in magnetic properties were not due to size effects. The ball-milled samples yielded particles much smaller and with a lower particle size distribution (**1-BM10** = 27 ± 11 nm and **1-BM90** = 22 ± 7 nm). The longer the duration of grinding, the smaller the particles obtained and the narrower the size distribution.

The significant differences between magnetic properties and PXRD patterns for **1-Sol** and the mechanically synthesised samples indicate that the β -phase is indeed a distinct polymorph. This was supported by exploring the potential effects of amorphisation, solvent contributions and particle size effects, yielding no significant contributions from these factors. Therefore, we report the application of mechanochemistry in the synthesis of the previously uncharacterised β -phase of [Fe(atrz)₃](BF₄)₂, yielding a polycrystalline powder without indication of the presence of the α -phase. Postsynthetic grinding of **1-Sol** was undertaken, and conversion of the α -phase to the β -phase was possible by manually grinding **1-Sol** in a pestle and mortar, yielding a 60% conversion in 10 min and an increase to 75% conversion after 30 min.

We have shown that synthetic and postsynthetic grinding can be used to access a different polymorph of a well-known and widely investigated SCO system. This highlights the potential for mechanochemistry to access entirely new materials that have not previously been isolated using solution-state techniques. However, it also shows that a degree of caution is required when applying this new approach. The effects observed may be specific to a particular system, and further investigation on

multiple systems should be undertaken before conclusions on the effects of synthetic and postsynthetic grinding are made.

Supplementary Materials: The following are available online at <http://www.mdpi.com/2312-7481/6/3/44/s1>, Figure S1: Plots of $\chi_M T$ vs T for compound **1-Sol** three cycles. Figure S2: Plots of $\chi_M T$ vs T for compound **1-Mech** three cycles. Figure S3: Plots of $\chi_M T$ vs T for compound **1-BM10** three cycles. Figure S4: Plots of $\chi_M T$ vs T for compound **1-BM90** three cycles. Table S1: Coordination spheres, interionic distances (R), variance of the absorber-scatterer distances (σ^2), energy shift (E_f) and quality of fit (R-fit) of the EXAFS data for (**1-Sol**, **1-Mech**, **1-BM10** and **1-BM90**). Figure S5: TGA plot of % mass vs temperature for **1-Sol**. Collected between 50–500 °C with a heating rate of 10 K/min. Figure S6: TGA plot of % mass vs temperature for **1-BM10**. Collected between 50–500 °C with a heating rate of 10 K/min. Figure S7: TGA plot of % mass vs temperature for **1-BM90**. Collected between 50–500 °C with a heating rate of 10 K/min. Figure S8: TGA plot of % mass vs temperature for **1-Mech**. Collected between 50–500 °C with a heating rate of 10 K/min. Figure S9: Additional TEM images for **1-Sol**. Figure S10: Additional TEM images for **1-Mech**. Figure S11: Additional TEM images for **1-BM10**. Figure S12: Additional TEM images for **1-BM90**. Figure S13: TGA plot of % mass vs temperature for **1-Sol-10**. Collected between 50–500 °C with a heating rate of 10 K/min. Figure S14: TGA plot of % mass vs temperature for **1-Sol-30**. Collected between 50–500 °C with a heating rate of 10 K/min.

Author Contributions: J.H.A. synthesized all complexes and analyzed all samples with the exception of EXAFS data. He also wrote the manuscript. D.M.P. and A.V.C. collected and analyzed EXAFS data. G.O.L. provided advice and expertise on mechanochemical synthesis via ball milling and contributed to project development. H.J.S. initiated and supervised the project, contributed to sample analysis and manuscript editing. All authors contributed to revising the manuscript. All authors have read and agreed to the published version of the manuscript.

Funding: This research was funded in part by Leverhulme Trust grant number RPG-2019-067.

Acknowledgments: G.O.L. would like to thank the Royal Society of Edinburgh/Scottish Government Personal Research Fellowship scheme while at Heriot-Watt University (HWU), Scotland. HWU is also thanked for hosting GOL and supporting this project. Hayley R. Green is thanked for assistance with the use of the Retsch M400 instrument. This project was supported by the HWU Energy Academy 2016 Fledge Award (Susana Garcia-Lopez and Filipe Vilela (HWU) are thanked for being a co-I on this grant). H.J.S. would like to thank the Leverhulme Trust (RPG-2019-067) for funding and the Diamond Light Source for the award of beam time as part of the Energy Materials Block Allocation Group SP14239.

Conflicts of Interest: The authors declare no conflict of interest.

References

- Sanchez Costa, J. Macroscopic methods: Magnetic, optical, and calorimetric techniques. *Comptes Rendus Chim.* **2018**, *21*, 1121–1132. [CrossRef]
- Gaspar, A.B.; Molnár, G.; Rotaru, A.; Shepherd, H.J. Pressure effect investigations on spin-crossover coordination compounds. *Comptes Rendus Chim.* **2018**, *21*, 1095–1120. [CrossRef]
- Chastanet, G.; Lorenc, M.; Bertoni, R.; Desplanches, C. Light-induced spin crossover—Solution and solid-state processes. *Comptes Rendus Chim.* **2018**, *21*, 1075–1094. [CrossRef]
- Zenere, K.A.; Duyker, S.G.; Trzop, E.; Collet, E.; Chan, B.; Doherty, P.W.; Kepert, C.J.; Neville, S.M. Increasing spin crossover cooperativity in 2D Hofmann-type materials with guest molecule removal. *Chem. Sci.* **2018**, *9*, 5623–5629. [CrossRef] [PubMed]
- Young, M.C.; Liew, E.; Hooley, R.J. Colorimetric barbiturate sensing with hybrid spin crossover assemblies. *Chem. Commun.* **2014**, *50*, 5043–5045. [CrossRef] [PubMed]
- Tissot, A.; Kesse, X.; Giannopoulou, S.; Stenger, I.; Binet, L.; Rivière, E.; Serre, C. A spin crossover porous hybrid architecture for potential sensing applications. *Chem. Commun.* **2019**, *55*, 194–197. [CrossRef] [PubMed]
- Senthil Kumar, K.; Ruben, M. Emerging trends in spin crossover (SCO) based functional materials and devices. *Coord. Chem. Rev.* **2017**, *346*, 176–205. [CrossRef]
- Manrique-Juárez, M.D.; Rat, S.; Salmon, L.; Molnár, G.; Quintero, C.M.; Nicu, L.; Shepherd, H.J.; Bousseksou, A. Switchable molecule-based materials for micro- and nanoscale actuating applications: Achievements and prospects. *Coord. Chem. Rev.* **2016**, *308*, 395–408. [CrossRef]
- Molnár, G.; Rat, S.; Salmon, L.; Nicolazzi, W.; Bousseksou, A. Spin crossover nanomaterials: From fundamental concepts to devices. *Adv. Mater.* **2018**, *30*, 1703862. [CrossRef]
- Molnár, G.; Salmon, L.; Nicolazzi, W.; Terki, F.; Bousseksou, A. Emerging properties and applications of spin crossover nanomaterials. *J. Mater. Chem. C* **2014**, *2*, 1360–1366. [CrossRef]

11. Dugay, J.; Giménez-Marqués, M.; Kozlova, T.; Zandbergen, H.W.; Coronado, E.; Van Der Zant, H.S.J. Spin Switching in Electronic Devices Based on 2D Assemblies of Spin-Crossover Nanoparticles. *Adv. Mater.* **2015**, *27*, 1288–1293. [[CrossRef](#)] [[PubMed](#)]
12. Gütlich, P.; Hauser, A.; Spiering, H. Thermal and optical switching of iron(II) complexes. *Angew. Chem. Int. Ed. Engl.* **1994**, *33*, 2024–2054. [[CrossRef](#)]
13. Matouzenko, G.S.; Bousseksou, A.; Borshch, S.A.; Perrin, M.; Zein, S.; Salmon, L.; Molnar, G.; Lecocq, S. Cooperative Spin Crossover and Order–Disorder Phenomena in a Mononuclear Compound [Fe (DAPP)(abpt)](ClO₄)₂ [DAPP=[Bis (3-aminopropyl)(2-pyridylmethyl) amine], abpt= 4-Amino-3, 5-bis (pyridin-2-yl)-1, 2, 4-triazole]. *Inorg. Chem.* **2004**, *43*, 227–236. [[CrossRef](#)] [[PubMed](#)]
14. Banerjee, H.; Chakraborty, S.; Saha-Dasgupta, T. Design and control of cooperativity in spin-crossover in metal–organic complexes: A theoretical overview. *Inorganics* **2017**, *5*, 47. [[CrossRef](#)]
15. Haddad, M.S.; Federer, W.D.; Lynch, M.W.; Hendrickson, D.N. An explanation of unusual properties of spin-crossover ferric complexes. *J. Am. Chem. Soc.* **1980**, *102*, 1468–1470. [[CrossRef](#)]
16. Haddad, M.S.; Federer, W.D.; Lynch, M.W.; Hendrickson, D.N. Spin-crossover ferric complexes: Unusual effects of grinding and doping solids. *Inorg. Chem.* **1981**, *20*, 131–139. [[CrossRef](#)]
17. Goodwin, H.A. Spin crossover—An overall perspective. *Spin Crossover Transit. Met. Compd. I* **2004**, *233*, 59–90.
18. Nieto-Castro, D.; Garcés-Pineda, F.A.; Moneo-Corcuera, A.; Pato-Doldan, B.; Gispert-Guirado, F.; Benet-Buchholz, J.; Galán-Mascarós, J.R. Effect of Mechanochemical Recrystallization on the Thermal Hysteresis of 1D FeII-triazole Spin Crossover Polymers. *Inorg. Chem.* **2020**, *59*, 7953–7959. [[CrossRef](#)]
19. Roubeau, O. Triazole-based one-dimensional spin-crossover coordination polymers. *Chem. A Eur. J.* **2012**, *18*, 15230–15244. [[CrossRef](#)]
20. Jonas, K.; Jean-Paul, A.; Renée, C.; Epiphane, C.; Olivier, K.; Haasnoot, J.G.; Françoise, G.; Charlotte, J.; Bousseksou, A.; Jorge, L.; et al. Spin transitions and thermal hysteresis in the molecular-based materials [Fe (Htrz)₂ (trz)](BF₄) and [Fe (Htrz)₃](BF₄)₂ · nH₂O (Htrz= 1, 2, 4-4H-triazole; trz= 1, 2, 4-triazolato). *Chem. Mater.* **1994**, *6*, 1404–1412.
21. Durand, P.; Pillet, S.; Bendeif, E.-E.; Carteret, C.; Bouazaoui, M.; El Hamzaoui, H.; Capoen, B.; Salmon, L.; Hébert, S.; Ghanbaja, J.; et al. Room temperature bistability with wide thermal hysteresis in a spin crossover silica nanocomposite. *J. Mater. Chem. C* **2013**, *1*, 1933. [[CrossRef](#)]
22. Goodwin, H.A. Spin Crossover—An Overall Perspective. In *Spin Crossover in Transition Metal Compounds I*; Springer: Berlin, Germany, 2004; pp. 1–47.
23. Kahn, O.; Kröber, J.; Jay, C. Spin transition molecular materials for displays and data recording. *Adv. Mater.* **1992**, *4*, 718–728. [[CrossRef](#)]
24. Varnek, V.A.; Lavrenova, L.G. Mossbauer study of the influence of ligands and anions of the second coordination sphere in Fe(II) complexes with 1,2,4-triazole and 4-amino-1,2,4-triazole on the temperature of the ¹A₁ ↔ ⁵T₂ spin transitions. *J. Struct. Chem.* **1995**, *36*, 104–111. [[CrossRef](#)]
25. Daro, N.; Moulet, L.; Penin, N.; Paradis, N.; Létard, J.F.; Lebraud, E.; Buffière, S.; Chastanet, G.; Guionneau, P. Spray-drying to get spin-crossover materials. *Materials* **2017**, *10*, 60. [[CrossRef](#)] [[PubMed](#)]
26. Kahn, O.; Martinez, C.J. Spin-transition polymers: From molecular materials toward memory devices. *Science* **1998**, *279*, 44–48. [[CrossRef](#)]
27. Grosjean, A. Matériaux Polymériques 1D à Transition de Spin: Investigations Structurales Multi-Echelles. Ph.D. Thesis, L’université Bordeaux, Bordeaux, France, 2013.
28. Askew, J.H.; Shepherd, H.J. Mechanochemical synthesis of cooperative spin crossover materials. *Chem. Commun.* **2018**, *54*, 180–183. [[CrossRef](#)] [[PubMed](#)]
29. Askew, J.H.; Shepherd, H.J. Post-synthetic anion exchange in iron (ii) 1, 2, 4-triazole based spin crossover materials via mechanochemistry. *Dalt. Trans.* **2020**, *49*, 2966–2971. [[CrossRef](#)]
30. Michalowicz, A.; Moscovici, J.; Ducourant, B.; Cracco, D.; Kahn, O. EXAFS and X-ray powder diffraction studies of the spin transition molecular materials [Fe(Htrz)₂(trz)](BF₄) and [Fe(Htrz)₃](BF₄)₂·nH₂O (Htrz= 1, 2, 4-4H-triazole; trz= 1, 2, 4-triazolato). *Chem. Mater.* **1995**, *7*, 1833–1842. [[CrossRef](#)]
31. Michalowicz, A.; Moscovici, J.; Kahn, O. Polymerie Fe(II) Spin Cross Over Compounds: XAS Structural Results. *Le J. Phys. IV* **2009**, *7*, C2-633–C2-635. [[CrossRef](#)]

32. Suleimanov, I.; Sánchez Costa, J.; Molnár, G.; Salmon, L.; Bousseksou, A. The photo-thermal plasmonic effect in spin crossover@ silica–gold nanocomposites. *Chem. Commun.* **2014**, *50*, 13015–13018. [[CrossRef](#)]
33. Michen, B.; Geers, C.; Vanhecke, D.; Endes, C.; Rothen-Rutishauser, B.; Balog, S.; Petri-Fink, A. Avoiding drying-artifacts in transmission electron microscopy: Characterizing the size and colloidal state of nanoparticles. *Sci. Rep.* **2015**, *5*, 9793. [[CrossRef](#)] [[PubMed](#)]



© 2020 by the authors. Licensee MDPI, Basel, Switzerland. This article is an open access article distributed under the terms and conditions of the Creative Commons Attribution (CC BY) license (<http://creativecommons.org/licenses/by/4.0/>).